https://doi.org/10.2352/ISSN.2470-1173.2017.20.3DIPM-006

Small scale surface profile recovery using a tunable lens based system

Ludovic J. Angot-Petit; Industrial Technology Research Institute; Chutung, Taiwan

Abstract

In the field of Automated Optical Inspection (AOI), measuring the 3D profile of objects can be of paramount importance, enabling the measure of surface roughness, critical small or large scale dimensions in x, y and z, radius of curvature; all of which requiring a high level of accuracy and repeatability. This paper presents a depth from focus surface profile recovery approach using a tunable lens. Two prototype systems and calibrations steps are detailed, several focus measures are introduced and implemented. Experimental results shows the applicability of the approach to small scale depth measurements and surface reconstruction.

Introduction

Depth from focus (DFF) and its counterpart, depth from defocus (DFD), are approaches used to obtain the depth profile of an object or a scene from a series of images captured at different focus distances (DFF) or under different focus conditions (DFD). These approaches saw their inception with the seminal paper from Pentland [1]. DFF and DFD have then been studied and implemented in both the academic [2, 3, 4, 5, 6, 7] and the industrial world [13]. The generally accepted difference between DFF and DFD is that in DFF the image capture parameters remain constant and focus distance changes (the camera moves along the depth axis), while with DFD the image capture parameters change (ex. lens aperture, lens focus, relative distance between the lens and the sensor,...) ([4, 5]). While these approaches allow high resolution measures (e.g. roughness, that is sub-micron scale 3D surfaces [13]), the time taken to acquire images is relatively long due to the scanning motion of the translation stage employed to vary the focus distance of the imaging system. The relatively recent introduction of electrically focal length tunable lenses allows capturing a stack of images without motion and at as high a speed as 10ms per images (e.g. [15, 16]), providing the camera permits such a frame rate. This paper describes the implementation of a tunable lens for motionless image capture at different focus heights and the inspected object profile reconstruction. From the difference between DFF and DFD discussed above, the present work can be seen as belonging to both categories: it is by nature DFF since the focus distance varies, but this variation isn't obtained by changing the physical distance between the object and the camera but by changing the tunable lens parameters. This paper identifies the main parameters deciding upon the accuracy of a depth measure: optical system performances, focus measure accuracy and system calibration. The optical system including a tunable lens is described in the first section, the second section introduces the image processing and several focus measures, while the two remaining sections are dedicated to system calibration and experimental results.

Optical system

An ideal optical system for DFF would have an infinitely small depth of field. Theory and practice of optics show however that the depth of field is limited by diffraction and the wave nature of light. Depth of field in air for a microscope objective can be well approximated by [10]:

$$\delta_z = \frac{\lambda}{NA^2} \tag{1}$$

where λ is the wavelength of the illumination source and NA the numerical aperture of the microscope objective. The resolving power in the object plane is

$$\delta_{xy} = \frac{1.22\lambda}{2NA} \tag{2}$$

Two prototype systems were built for this study, each comprising a main imaging lens and a tunable lens. Both systems implement a microscope lens, the difference being that one uses an infinite conjugate microscope lens while the other uses a finite conjugate microscope lens. Explanations about the differences between infinite and finite conjugate microscope lenses can be found in [11]. Since the microscope lens isn't used on its own but together with other optical elements, the above formula only gives an approximation to the depth of field. Also, the depth of field is not an absolute value where anything outside the above defined depth of field is out of focus and everything within is in focus: within the theoretical depth of field, variation of focus can be observed. Using a blue light of wavelength 470nm, the microscope objective used in the finite conjugate system having a NA=0.1, the depth of field given by eq.1 is 47µm (noting this is for the microscope lens itself, the depth of field for the whole system was measured with an inclined ronchi ruling target to be about 40µm). It will be shown that with an appropriate system calibration, a depth resolution higher than this theoretical depth of field can be obtained.

In addition to an ideally narrow depth of field, the best optical configuration for DFF is a telecentric optical system [19], for which the property of interest is that the magnification ratio remains constant over a range of distances from the lens to the object. There are several ways to obtain a telecentric system, the first one being to use a telecentric lens, two other approaches are explored in this study. The first one is based on a finite conjugate microscope lens and inspired by the work in [12], while the second approach employs an infinite conjugate microscope lens described in [18] for light sheet microscopy applications. While both systems were assembled, built and tested, the former was used for the experiments reported in this article and for comparison with an existing metrology system, the Keyence VR3000 series; the reason being that their magnification ratios and depth resolutions are comparable. The infinite conjugate lens based system

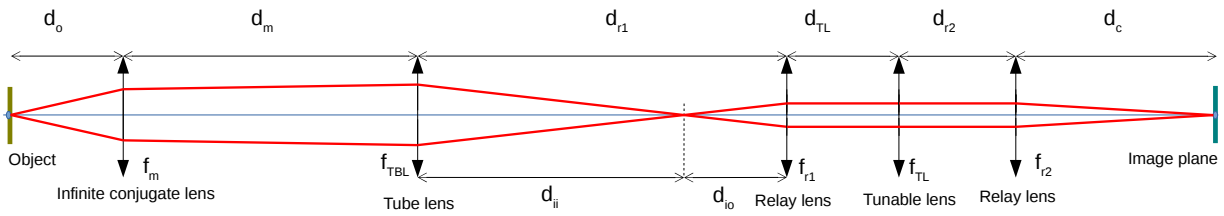

Figure 1: Infinite conjugate lens based tunable lens optical system diagram.

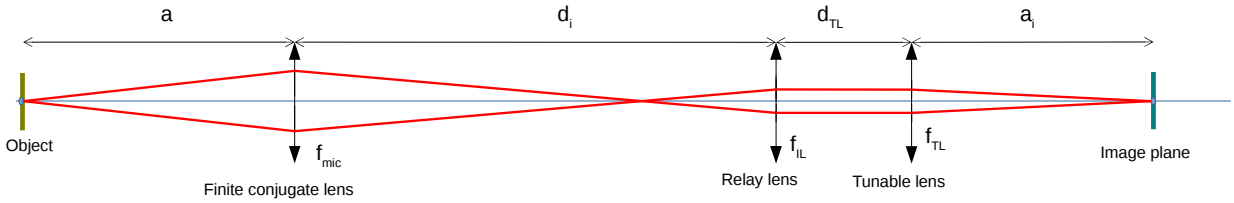

Figure 2: Finite conjugate lens based tunable lens optical system diagram.

is shown in fig.1. It consists in an infinity corrected microscope lens (Nikon L-plan 10x), a tube lens (Thorlabs ITL200), a relay lens, the tunable lens, another relay lens and a camera. The use of an infinite conjugate lens permits the introduction of a beam splitter in the optical path for coaxial illumination. The tunable lens is located at the back focal plane of the objective lens, which corresponds to the Fourier transform of the exit pupil of the objective lens. The placement of the relay lenses and tunable lens corresponds to that of a 4-f system.

The finite conjugate lens based system requires less elements than the infinite conjugate system and is more compact (fig.2). It comprises a finite corrected microscope lens (Nikon plan 4/0.1 160/), an intermediate lens, the tunable lens and a camera. Contrary to the infinite conjugate based system, the finite conjugate system doesn't allow the introduction of a coaxial light in the imaging path, a ring light is used as the light source.

Tunable lens

An electrically focus tunable lense (EFTL), also known as liquid lense or more simply as tunable lense (TL), is a single optical element for which the radius of curvature (equivalently, the focal length) can be changed electrically. They are classified depending on the material of the lens itself and the technology used to vary their focal length. Polymer based tunable lenses are controlled by a current which changes the radius of curvature of a polymer material (optotune, [15]). The other main class of tunable lenses are based on the concept of electro-wetting, where the electrical control parameter is a voltage (varioptics, [16]), changing the radius of curvature of an optically transparent liquid material. The present work was carried out with the Optotune tunable lens model EL-10-30-C. The control of the tunable lens is performed by a high precision current source. A custom made current source was designed to be compatible with Arduino development boards. The high precision current source integrated circuit (IC) is based on the ADN8810, the same component as implemented in Optotune's own lens controller. The ADN8810 data sheet explains the relationship between the IC current control code and the output current, which depends on only a small number of external components. The interesting property of using this IC together with the tunable lens is that the relationship between the optical power (i.e. the inverse of the focal length) of the tunable lens and the current source control code is linear. The following section will show that in addition, there is a linear relationship between the tunable lens's optical power and the focus distance, it will then be possible to capture images at well defined focus distances, by setting the appropriate control current. The tunable lense used in this project is a temperature sensitive device, it should be used in a temperature controlled environment and allowed to warm-up for an appropriate period, if the temperature varies during the measurement, a proper calibration should be carried out in order to correct the influence of temperature on the EFTL's focal length.

System analysis

This section explains how the relationship between the focus distance and the tunable lens optical power (the inverse of the focal length) is obtained. The analysis of the optical systems is done with matrix optics under the paraxial approximation, and while this is not the most accurate way to modelize an optical system, it provides a good indication of the relation between the main physical parameters involved. The ABCD matrix for the finite conjugate is:

$$[M_{FC}] = \begin{bmatrix} 1 & a_i \\ 0 & 1 \end{bmatrix} \begin{bmatrix} 1 & 0 \\ \frac{-1}{f_{TL}} & 1 \end{bmatrix} \begin{bmatrix} 1 & d_{TL} \\ 0 & 1 \end{bmatrix} \begin{bmatrix} A_{IL} & B_{IL} \\ C_{IL} & D_{IL} \end{bmatrix} \times \begin{bmatrix} 1 & d_i \\ 0 & 1 \end{bmatrix} \begin{bmatrix} 1 & 0 \\ \frac{-1}{f_{mic}} & 1 \end{bmatrix} \begin{bmatrix} 1 & a \\ 0 & 1 \end{bmatrix} \quad (3)$$

where a is the distance between the object and the imaging lens of focal length f_{mic}, d_i the distance between the imaging lens and the imaging lens, separated from the tunable lens by d_{TL}, the tunable lens focal length is variable and noted f_{TL}. a_i is the distance between the tunable lens and the image plane (fig.2). The intermediate lens can be a single bi-convex lens or an achromatic lens, hence the more general notation for the ABCD matrix for the intermediate lens. When the magnification ratio doesn't depend on the focus distance, the system has the important property of a telecentric lens: its magnification ratio remains constant over a range of distances. Eliminating the dependence on the focal length for

the constant magnification condition, the magnification ratio can be found to be :

$$m_{FC} = a_i(C_{IL}[1 - d_i P_{mic}] - D_{IL}P_{mic}) \tag{4}$$

where $P_{mic} = \frac{1}{f_{mic}}$. The working distance is then:

$$a = \frac{-B_{lenses} - a_i D_{lenses}}{a_i C_{lenses}} \tag{5}$$

where $B_{lenses} = A_{IL}d_i + B_{IL} + d_{TL}[C_{IL}d_i + D_{IL}]$, $C_{lenses} = C_{IL}[1 - d_i P_{mic}] - D_{IL}P_{mic}$ and $D_{lenses} = -P_{TL}B_{lenses} + C_{IL}d_i + D_{IL}$. The relationship between the focus distance is thus of the form:

$$a = \alpha P_{TL} + \beta \tag{6}$$

where α and β are constants depending on the characteristics of the optical system. Eq.6 shows that the working distance (i.e. focus distance) and the optical power P_{TL} of the tunable lens follow a linear relationship, as will be demonstrated experimentally in section on system calibration. In the case of the Optotune tunable lens, P_{TL} is itself proportional to the control current applied to the lens, hence, the focusing distance a also follows a linear relationship with the tunable lens control current.

The matrix analysis for the infinite conjugate based optical system follows the same principles but is more tedious; calculation are simplified by splitting the system into two subsystems, one comprising the imaging lens and the other the tunable lens. Main results are reported below. The system is a 4-f system, that is:

$$f_{r1} = f_{r2} = d_c = d_{r2} = d_{TL} = d_{4F} \tag{7}$$

where f_{r1} and f_{r2} are the focal length of the relay lenses, and the distances are defined on fig.1 as follows: d_c is the distance from the camera sensor to relay 2, d_{r2} the distance between relay lens 2 and the tunable lens, d_{TL} is the distance between the tunable lens and the relay lens 1. Taking into account the condition expressed in eq.7 and setting a magnification ratio m_{IC} independent from the focus distance d_o, one can obtain an expression for the variation of the focus distance Δd_o as a function of the tunable lens optical power ΔP_{TL}:

$$\Delta d_o = -\frac{\Delta P_{TL} d_{4f}^2}{m_{mic}^2} \tag{8}$$

where P_{TL} is the optical power (diopter) of the tunable lens. For the infinite conjugate system the focus distance is therefore also a linear function of the lens' optical power, itself a linear function of the lens' control current.

Focus measure and depth reconstruction

A focus measure can be seen as an operator indicating the amount of sharpness in an image at a given pixel location. The difficulty in evaluating the focus is multifold: focus measure depends on the texture of the object, the object illumination, the noise present in the captured image (which itself depends on other various factors such as camera gain, light intensity,...), the imaging system resolution, ... Providing an ideal optical system with an infinitely small depth of field, an ideal focus measure would behave as a Dirac impulse function: equal to 1 when the object is in focus, 0 otherwise. Such ideal optical system doesn't exist, neither does such ideal focus measure, and this is related to the finite impulse response of any optical system, described by its Point Spread Function (PSF). A thorough comparison of focus measures is done by Pertuz et al. in [6]. For each focus measure used in this study and detailed below, (x,y) is the location at which sharpness is evaluated and I the domain of interest of dimensions (M,N) over which focus is evaluated.

Sum of Squared difference (SSD)

The Sum of Squared Difference (SSD) is a well known distance measure operator, used for example in template matching. It is introduced here as a focus operator:

$$\Phi_{SSD}(I(x,y)) = \sum_M \sum_N [I(x,y) - I(x+s_x, y+s_y)]^2 \tag{9}$$

The steps s_x and s_y are chosen to be one pixel, and the domain over which the SSD is applied is the sub-window centered on the pixel at location (x,y) where sharpness is evaluated. The idea is here that the sum of square difference between an image, or sub-window, and a copy of itself shifted in X and Y by 1 pixel is all the larger as the image contains high frequency information. For a very blur image, the difference between the image and its shifted copy is close to zero.

Variance Of Laplacian (VL)

Variance of Laplacian was first introduced in [17] and was compared to other focus measure in [6]. Laplacian based operator shows the best overall performance in normal image conditions, but the addition of noise tends to degrade the performance of these operators. This can be expected at small scale (high magnification ratio), where the structure and texture of the object present noise like variations. Variance of Laplacian is implemented as:

$$\Phi_{VL} I(x,y) = \frac{1}{MN} \sum_M \sum_N [\Delta I(x,y) - \overline{\Delta I(x,y)}]^2 \tag{10}$$

where $\Delta I(x,y)$ is the Laplacian of the area of interest I:

$$\Delta I(x,y) = \frac{\partial^2 I}{\partial x^2} + \frac{\partial^2 I}{\partial y^2} \tag{11}$$

Tenengrad (Ten)

The Tenengrad operator is computed by applying the Sobel operator to the image or a sub-window centered on the pixel of interest ([12, 17]):

$$\Phi_{TEN}(I(x,y)) = \sum_M \sum_N [S(x,y)]^2 \tag{12}$$

where

$$S(x,y) = \sqrt{[G_x(x,y)]^2 + [G_y(x,y)]^2} \tag{13}$$

with $G_x(x,y)$ and $G_y(x,y)$ being the result of the Sobel operator applied to the area of interest I respectively along the x and the y direction.

Normalized Gray Level Variance (NGLV)

This operator is introduced in [17], it measures the variance of the grey level intensity across the image and is normalized to the averaged grey level in the image or region of interest:

$$\Phi_{NGLV}(I(x,y)) = \frac{1}{\mu MN}\sum_M\sum_N [I(x,y)-\mu]^2 \tag{14}$$

where $\mu = \overline{I(x,y)}$ is the average intensity in the sub-window centered on pixel x,y.

Modified Laplacian (ML)

This operator was first introduced in [8] to overcome the case where the Laplacian operator cancels out in particular situation where the texture in the object leads to opposite signs of the partial second derivative in x and in y.

$$\Delta_{ML} I(x,y) = \left|\frac{\partial^2 I}{\partial x^2}\right| + \left|\frac{\partial^2 I}{\partial y^2}\right| \tag{15}$$

The modified Laplacian based focus operator is calculated by a discrete approximation of eq.15:

$$\Phi_{ML} I(x,y) = \sum_M\sum_N |2I(x,y) - I(x-s_x,y) - I(x+s_x,y)| + \left|2I(x,y) - I(x,y-s_y) - I(x,y+s_y)\right| \tag{16}$$

As for the SSD operator, the steps s_x and s_y have also been chosen to be 1 (also the choice of [6]), but experimentation can be carried to evaluate the performances of this operator for other step sizes.

Variance of Gaussian of Laplacian (VGL)

Laplacian is sensitive to noise and so is variance of Laplacian, the rational is here to compute the Laplacian of the region of interest, apply a Gaussian filter to the Laplacian, and compute the variance of the obtained Gaussian of Laplacian.

$$\Phi_{VGL}(I(x,y)) = \frac{1}{MN}\sum_M\sum_N [\Gamma(\Delta I) - \overline{\Gamma(\Delta I)}]^2 \tag{17}$$

where Γ is a Gaussian filter operator.

The remaining focus measures described below consist in evaluating the focus variation along the z-axis direction over a segment of length sw_z at each I_z, the area of interest at depth z. In other words, these focus measures are computed in a 3D sub-window.

Variance of Laplacian of Tenengrad (VTEN)

Variance of Laplacian is known to be sensitive to noise, while Tenengrad is much less sensitive to noise. The idea arose then to combine both operator: apply the Tenengrad operator in a sub-window of the image and then apply a Variance of Laplacian along the z axis, that is along the stack of captured images. A one dimensional variance of Laplacian is applied to the two dimensional focus measure, as:

$$\Phi_{VTEN}(I(x,y)) = \sum_{sw_z} [\Delta\Phi_{TEN}(I_z) - \overline{\Delta\Phi_{TEN}(I_z)}]^2 \tag{18}$$

3D Variance of Laplacian (VVL)

3D variance of Laplacian can be see as a one dimensional z Variance of Laplacian applied to the Variance of Laplacian applied to a single plane. It is expressed as:

$$\Phi_{VVL}(I(x,y)) = \sum_{sw_z} [\Delta\Phi_{VL}(I_z) - \overline{\Delta\Phi_{VL}(I_z)}]^2 \tag{19}$$

Variance of Laplacian of Sum of Square Difference (VSSD)

Here, following the same principle as for Vten and VVL, VSSD consists in applying a variance of Laplacian along the z-axis for a series of SSD focus operators applied to a series of areas of interest. It is expressed as:

$$\Phi_{VSSD}(I(x,y)) = \sum_{sw_z} [\Delta\Phi_{SSD}(I_z) - \overline{\Delta\Phi_{SSD}(I_z)}]^2 \tag{20}$$

The concept of variance of Laplacian along the Z axis can be applied to any other focus measure operator, it allows measuring the variation of the defocus along this direction.

Depth reconstruction

An efficient approach to obtain a 3D profile of an object using DFF is described in [9]: it consists in applying a focus operator at pixel level, obtain a measure of the focus at each pixel, and, assuming a Gaussian model for the defocus of the image capture system, obtain the depth at each pixel with the highest focus by interpolating a Gaussian defocus model at these pixels locations. In this study Gaussian defocus model of the imaging system aren't required, depth maps are obtained by spatially filtering pixels with the highest focus at each image in a stack of images captured at different focus distances. The amount of focus is measured by one of the focus measure presented in the previous sections. A stack of in-focused regions of interest (ROI) is then obtained, from which the surface profile of the object is reconstructed.

System calibration

Calibration of the system is essential for any metrology application. The proposed calibration approach requires the imaging system to be mounted on a translation stage so that the distance between the lens and a reference surface can be varied. The translation stage used here is a high precision 1µm resolution manual vertical stage (Thorlabs). Calibration is performed as follows: at each regularly spaced position defined by the vertical translation stage, a series of images is captured at different focal length setting of the tunable lens. For each captured image a focus measure is computed. This results in a series of Gaussian-like curves as shown on fig.3 where the Tenengrad focus measure was used to illustrate the calibration principle. If the focus measure accurately detects the plane of best focus, then the maximum of each Gaussian-like curves, obtained at a particular current setting of the tunable lens, should match the corresponding height setting of the micrometer. A correspondence between the control current applied to the tunable lens and the height at which the optical system focuses can then be established, and the plot of fig.4 shows that the relationship between the control current applied to the tunable lens and the height at which the system focuses is linear.

Such linear relationship had already been established in eq.6. On fig.4, the ground truth height points are the actual height as dialed on the micrometer stage (0, 50µm, 100µm, ...) corresponding to the local maximum of the Gaussian-like curves of the series of calibration curves in fig.3; and the linear fit is the regression line fit of heights to these local maxima. The correlation coefficient of the linear regression is 0.9999, the absolute residual error between the ground truth and the linear regression is +/-3µm. This means that when using the linear regression fit as the calibration line for the system, the error on the focus height when using the Tenengrad operator is at most 3µm above or below the actual (ground truth) height. It should be noted that the calibration has to be performed for the focus to be used for the surface reconstruction.

Calibration as described previously was done manually, and is a time consuming operation. It can however easily be automatized, using a motorized translation stage and the appropriate control program. Automatic calibration is expected to take no more than one minute.

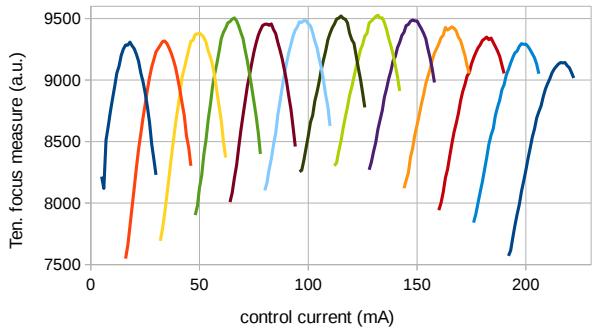

Figure 3: Focus measure (Tenengrad) sweep as a function of tunable lens control current for different focus height. Each bell shaped curve corresponds to a sweep of the tunable lens focal length at different height settings, separated by 50um steps

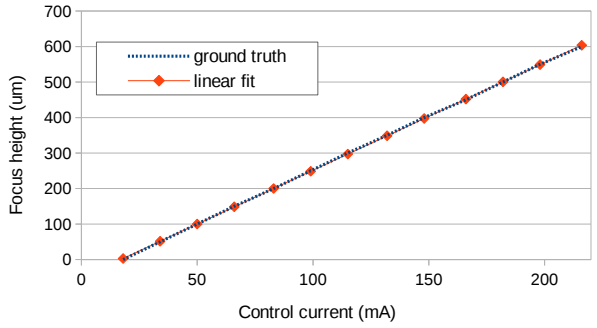

Figure 4: System calibration curve: focus height as a function of the tunable lens control current. Ground truth corresponds to the actual height dialed on the micrometer translation stage.

The following fig.5 and 6 show the comparison between all the focus measures previously introduced. Each curve corresponds to the focus measured in a region of interest of a reference flat surface over a focus distance sweep controlled by the tunable lens (that is without physically changing the working distance). Each focus measure was normalized, and since 3D focus measures additionally require a z-axis sweep, the focus measures were located over a common reference distance. Best focus measures are those with the highest variation (from defocus to in-focus) and the narrowest full width at half maximum (FWHM). The 2 points depth measurement experiment, detailed in a later section (results in table 1), shows indeed that for example the VSSD focus measure has the narrowest FWHM and the lowest height standard deviation. On the contrary, ML, VVL and VL display a noisy variation on fig.6 and present the largest height standard deviation.

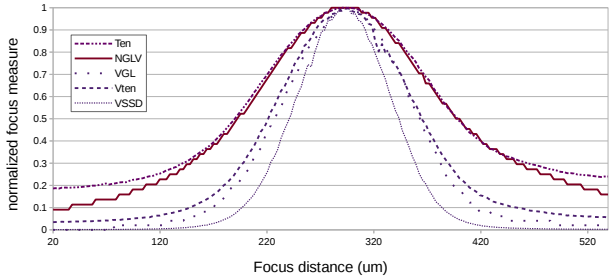

Figure 5: Focus Measures with FWHM $<$ 180µm

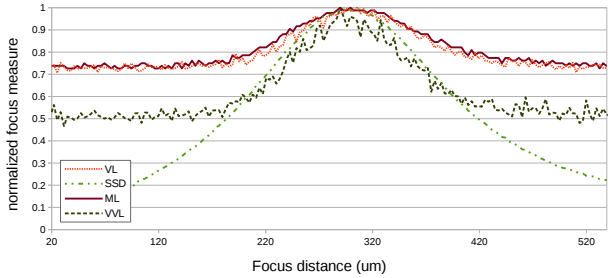

Figure 6: Focus Measures with FWHM $>$ 180µm

Optical Aberration correction

The finite conjugate system suffers from optical aberrations, the most noticeable one being spherical aberrations: when imaging a flat object, the center of the image is in focus while the outside of the image is slightly defocused. This is visually noticeable over a large area of interest such as the full camera field of view. Since such aberration introduces a defocus, they result in depth measurement error when using a DFF approach. Redesigning the optical system, for example with the introduction of aspherical elements, can be a path to follow to reduce the aberrations. Another solution is to compensate for the defocus effect associated to spherical aberration by another calibration step. The later was implemented: the depth map of a flat portion of the calibration target shown in fig.11a was obtained, and a correction matrix computed in order to compensate for the defocus introduced by the spherical aberrations. The uncorrected depth map of the flat surface is shown in fig.7.

Experimental results

A first set of experiments consisted in measuring the height of a calibrated step by a two point depth measurement approach, while the second set of experiments consisted in reconstructing the surface profile of a blind hole. The experiments were performed with the finite conjugate system, which magnification ratio is 4.3. Paired with a 3.5µm pixel size, one camera pixel represents 0.8µm in the object plane. The maximum height range

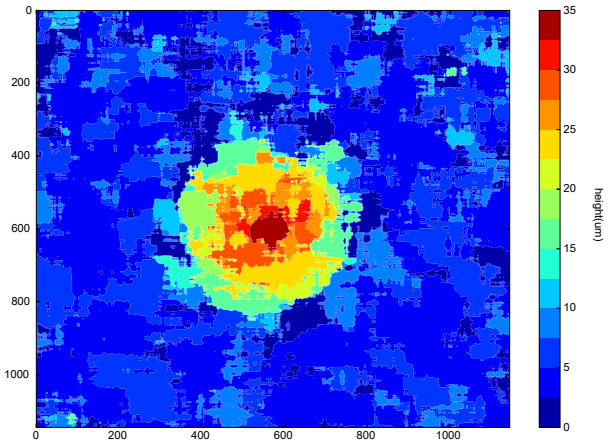

Figure 7: Raw depth map of a flat datum surface, used for calculating a matrix for optical aberration correction

over the full 290mA current range of the tunable lens is 700µm. The camera pixel count is 2448x2048 providing a field of view (FOV) of about 2mmx1.6mm. The border of the full FOV image is affected by optical distortions and the effective usefull FOV is 1.3mmx1.3mm. For depth map calculation, hardware binning was set on board the camera (pixels are grouped by 2x2), thereby increasing light sensitivity and frame rate. Equivalent pixel resolution in this case is 1.6µm, the FOV remains unchanged.

Two points depth measurement

The reference calibration target Keyence OP-87710 seen in fig.11a was used for this experiment. The ceramic portion of the target has two steps of respectively 2mm and 200µm height. The 200µm step was used for this experiment. The target is provided with the Keyence Macroscope VR series of depth measurement instrument, and comes with a calibration report and certificate, indicating that calibration measurement was done with a coordinate measuring machine model PRISMO 9/24/7 made by Tokyo Seimitsu, with reported height varying between 197.5µm and 198.4µm with a +/-5 µm tolerance. The two points depth measurement consists in setting two regions of interest (ROI) over the two adjacent surfaces of the step. The tunable lens is then controlled to perform a scan over the height of the step. The focus measure variation in each one of the ROI shows a peak corresponding to the height at which the associated captured image was in focus, the height of the step can thus directly be read from the focus measure variation in the ROI as shown in fig.8, taking into account the calibration performed previously. The curve shows slight local variations near the maximum of each focus measure, which can be supposed to contribute to the measurement error. These local variations can come from that the tunable lens focal length wasn't in a stable state after a current jump, or come from noise in the image, detected as changes in focus. In order to assess the origin of these variations, the tunable lens was offered an ample resting time of 100ms between each control current settings. No significant change in the error was noticed. Another test consisted in taking 10 measurements for each focus measure, computing an average calibration ratio from these 10 measurements and, using the obtained average calibration ratio, computing the height standard deviation over these 10 measurements. The sub-window size was a 111 pixels square and images were captured every 1µm. The local variations were eliminated, indicating that for an in-focus image, noise in the image is a major contributor to local variations of the focus measure. This test also shows the respective performances of the focus measures and results are reported in table 1. The VSSD focus measure has the smallest standard deviation of 3.65 µm over the 10 measurements, followed by the Tenengrad operator and SSD, while ML, VVL and VL have the largest standard deviation, making these operators unfit for this case where the object (the calibration target) have little texture. Figure 12 shows side by side the texture of the ceramic material used in the Keyence target (fig.11a) and the texture of the aluminum target (fig.11b), for the same 0.3x0.3mm FOV and under the same magnification ratio as the one used for all the experiments reported (4.3x). At this magnification ratio the ceramic appears smoother than the aluminum, which can explains the poor performance of the Laplacian based focus measures (ML, VL and VVL). An interesting future work would be to assess the optimum focus measure to use for a given material or surface texture. The surface texture could be quantified with means of statistical parameters such as, but not limited to, rugosity.

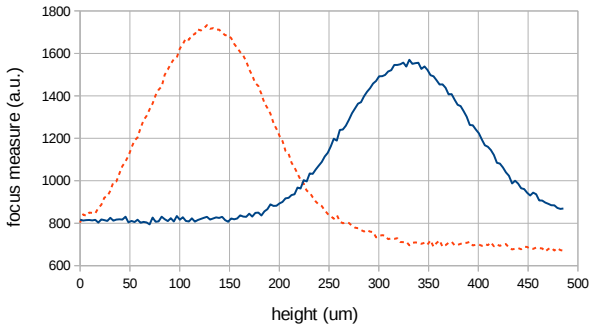

Figure 8: Two points depth measurement of a 200µm step: focus measure variation in two adjacent ROI locations of the step.

Surface profile reconstruction

This series of experiments consist in reconstructing the profile of a 500µm deep, 1mm diameter blind hole, shown in fig.11b. The tunable lens current control increment step was set so that each image is captured every either 10µm or 30µm height steps. Depth maps for two different FOV are reported, namely for the entire hole and for a narrower FOV corresponding to one quarter of the area of the hole. The entire hole depth maps were compared with those output by a high precision measurement system, the structured light based Keyence VR3000 system. In its high magnification ratio setting, the system has a 1.9x1.4mm FOV, a maximum measurable height of 1mm and a claimed 0.1µm height resolution [14]. Its companion software can output 3D data in world coordinates so that this 3D data and that output by the present approach could be compared, these sets of data were then imported into a visualization program written in Python. Both sets of data were converted into depth maps using the same parameters. Given the different magnification ratio and field of view between the proposed system and the Keyence system, and, most importantly, the absence of reliable fiducial markers on the test object for alignment and image registration, depth maps are here compared qualitatively. Also, it was noticed that some details of the object were not visible in the Keyence depth map and therefore

Table 1: Two points depth measurement focus measure performance comparison. Calibration coefficient K_{TL} is calculated based on a 200µm calibrated reference height, and the height standard deviation σ_H indicates the measured height variation in a set of 10 measurements

Focus measure	VSSD	Ten	SSD	VGL	NGLV	VTen	ML	VVL	VL
K_{TL} (µm/mA)	3.24	3.18	3.15	3.15	3.18	3.18	3.15	3.22	3.17
σ_H (µm)	3.65	4.96	5.70	6.16	6.23	7.78	27.13	33.53	46.57

the 3D data of this system couldn't be used as reference ground truth data. Other system such as confocal scanning microscope or chromatic confocal probes could be used to obtain a ground truth depth map but were not accessible at the time this study was made. Future work is planned to focus on a quantitative comparison by means of peak signal-to-noise ratio (PSNR) and mean square error (MSE). The depth map of the entire hole obtained by the proposed system is shown in fig.9, while that obtained by the Keyence system is shown in fig.10. Compared to the structured light system, the tunable lens based DFF approach offers more details of the edge of the hole, in particular, burrs can be clearly seen in the optical image and the depth map obtained with the proposed approach while they are less visible on the Keyence VR3000 even at its highest magnification ratio (burr visible on fig.13a, 9 and 14a). The depth maps presented in fig.9, obtained using the tenegrad operator, have only been corrected using the optical aberration correction matrix and appropriately scaled to share the same color bar scale as that of fig.10. The 3D data output by the Keyence system corresponds to a larger FOV than that of the proposed system, hence the difference in the origins of the X and Y axes.

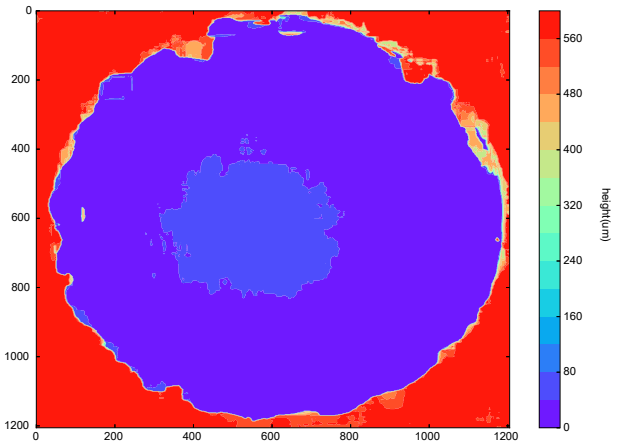

Figure 9: Depth map obtained with the tunable lens based system, tenengrad focus measure in a 61x61 pixel sub-window. XY dimensions are in µm.

Without changing the magnification ratio of the optical system, depth maps were then obtained for the smaller FOV. The optical image of this area of interest is shown in fig.13 for two focus positions. Three different sub-window sizes (over which the focus measure is evaluated at each pixel) were used in order to evaluate their influence on the depth map, for three focus measures, Tenengrad, VL and SSD, for a depth resolution of 10µm. Depth maps obtained with the SSD focus measure were also computed for a depth step of 30µm. No post processing is applied to these depth maps, and optical aberrations are not corrected (spherical aberrations are negligeable in this smaller FOV). All depth maps were obtained for the same position of the object and within the same half a day. Results are shown in fig.14.

The relationship between the size of the sub-window, magnification ratio and object texture can be intuitively understood: given a fixed magnification ratio for which the object's small scale texture is visible (any material have a texture, it is a matter of magnification ratio to be able to detect it), focus measured in large sub-windows has the positive effect to average the object's texture but the undesired effect to smooth sharp variations of the object's structure. Focus evaluated in small sub-windows has the exact opposite effects, and the small scale texture of the object can give rise to local depth variations where the surface is actually flat. The sub-window dimension should therefore be appropriately chosen, and adapted to the spatial period of the object texture as it appears in the captured image. Evaluating the frequency content of the object texture could be used as a parameter to set the size of the sub-window.

In all the depth maps in fig.14, the presence of a burr at a depth lower than the top surface of the hole is detected, even with depth maps obtained with the VL focus measure, which performed the worst in the two points depth measurement experiment. In all cases, depth maps obtained with the smallest sub-window are noisy in all three X,Y and Z dimensions, and would require post processing (e.g. outlier rejection, special implementation of a bilateral filter). On the other hand, larger sub-window require little to no post processing. However, as can be expected, the contour of the burr appears smaller and smoother for a larger sub-window size: the depth map obtained with the 61x61 sub-window doesn't reflect the actual dimensions of the burr (neither that of the contour of the hole itself). Using edge and contour information from the optical image could prove usefull in im-

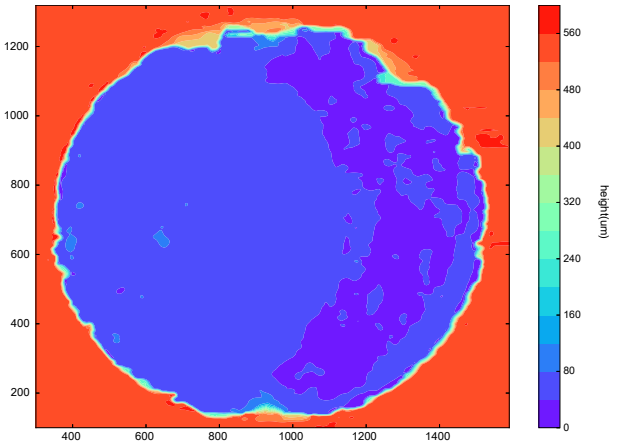

Figure 10: Depth map obtained with the structured light Keyence VR3000 system, XY dimensions are in µm

(a) Step height (b) Blind hole

Figure 11: Objects used for the experimentations: two points depth measurement (left) and surface reconstruction (right). A 0.5mm pencil lead shows the areas of interest and the objects' scale

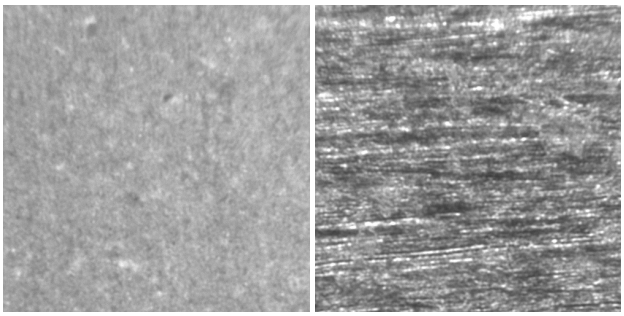

(a) ceramic (b) aluminum

Figure 12: Texture of the ceramic target shown in fig.11a and the aluminum object shown in fig.11b (0.3mmx0.3mm FOV, 4.3x magnification ratio)

proving the XY accuracy when larger sub-window sizes are used. Little difference is noticeable when comparing depth maps obtained with the two different focus measure. Figure 14d shows depth maps obtained with the SSD focus measure for a decreased Z resolution (30µm instead of 10µm). The computation time was notably reduced, being 12s, 29s and 88s for sub-window sizes of 5, 15 and 31 respectively without major difference in depth map appearance, the depth map at 10µm depth resolution showing more local depth variations. But at this lower depth resolution, any detail smaller (in depth) than the focus step of 30µm can't be detected.

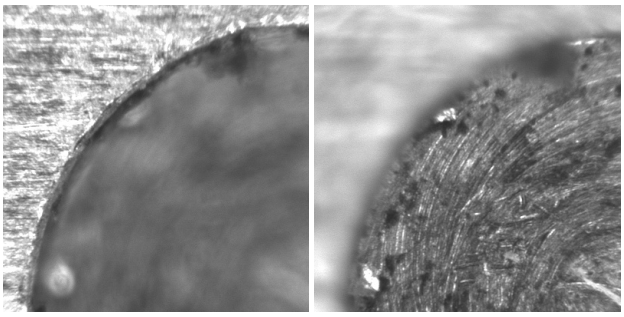

(a) Focus on top (b) Focus on the bottom

Figure 13: Portion of the blind hole (fig.11b) used for the 3D surface profile reconstruction experiments. Field of View is 0.64mmx0.64mm, optical system magnification ratio is 4.3

Computation time

Computation time necessary to reconstruct the surface profile of the same area of interest as in the previous section a 640µmx640µmx500µm volume at 1.6µm resolution in XY (equivalent pixel resolution) and 10µm in Z is reported in table 2 for all focus measures. It shows that depth maps are obtained with the NGLV focus measure in by far the shortest time (3 times faster than the second fastest), while the slowest computation times are for depth maps obtained with SSD based focus measures. The CPU was an intel i5 clocked at 1.6GHz.

The computation time for the depth maps shown in fig.14a was 117s, 141s and 208s for sub-window sizes 5, 15 and 31 pixels respectively. Depth maps in fig.14d were obtained with a 3 times lower spatial sampling rate along the Z dimension (30µm vs 10µm). The computation time was notably reduced, being 12s, 29s and 88s for the same respective sub-window sizes and this without any significant difference in depth map appearance. But any detail smaller (in depth) than the focus step of 30µm couldn't be detected or would give rise to inaccurate depths. These results shows the slowness of the depth map computation, however several aspects of this study should be kept in mind. The XY resolution is high (1.6µm), corresponding to a high spatial sampling rate, which may not be required and certainly can be optimized. Second, according to the results shown in fig.14d, the depth sampling rate can be optimized, in particular following the work in [20]. Finally, the depth map computation approach presented in this study is particularly well suited to parallel computing, and at least one order of magnitude speed increase is to be expected by using the processing power of modern graphical processing units (GPU).

Conclusion and future work

This study introduced the implementation of a small scale surface reconstruction system using a tunable lens, based on the principle of depth from focus (DFF). The optical system was analyzed using matrix optics, a calibration method was presented and several focus operators were compared. Correction for optical imperfection of the system, essentially spherical aberrations, was performed. Experiments with a calibrated target showed the system is accurate for 2 points depth measurement, and depth maps obtained with the system are qualitative on par with those obtained with a structured light based depth measurement metrology instrument. Depth map computation time for each focus measure was investigated and direction were given for its reduction. Future work will focus on exploring new approaches to 3D image processing, decreasing computation time and reducing aberrations in the optical system. Also, for the system to be used as a metrology instrument, Gage Repeatability and Reliability (GR&R) should be carried out in order to identify the parameters influencing the accuracy of the instrument.

References

[1] A.P. Pentland; A new sense to depth of field; IEEE Transactions on Pattern Analysis and Machine Intelligence, 9 pp. 523531 (1987).

[2] P. Favaro and S. Soatto; Learning shape from defocus; Proc. IEEE European Conference on Computer Vision; (2002).

[3] J. Ens and P. Lawrence; An investigation of methods for determining depth from focus; IEEE Trans. Pattern Anal. Mach. Intell.; 15, pg 97-108 (1993).

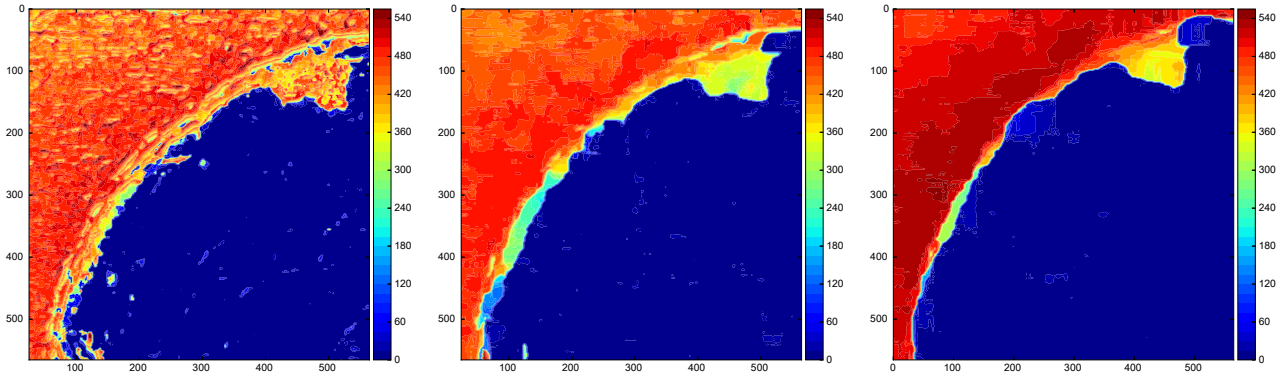

(a) Tenengrad (Ten), Z resolution = 10µm

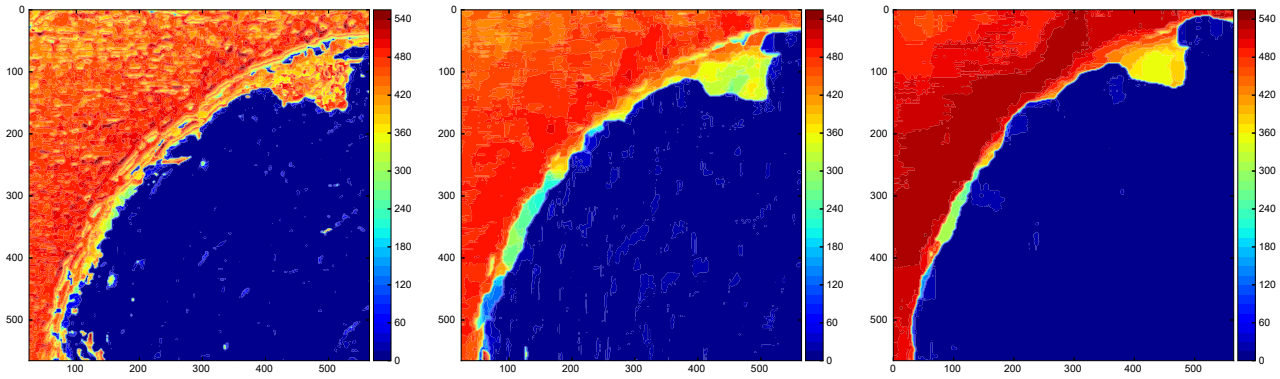

(b) Variance Of Laplacian (VL), Z resolution = 10µm

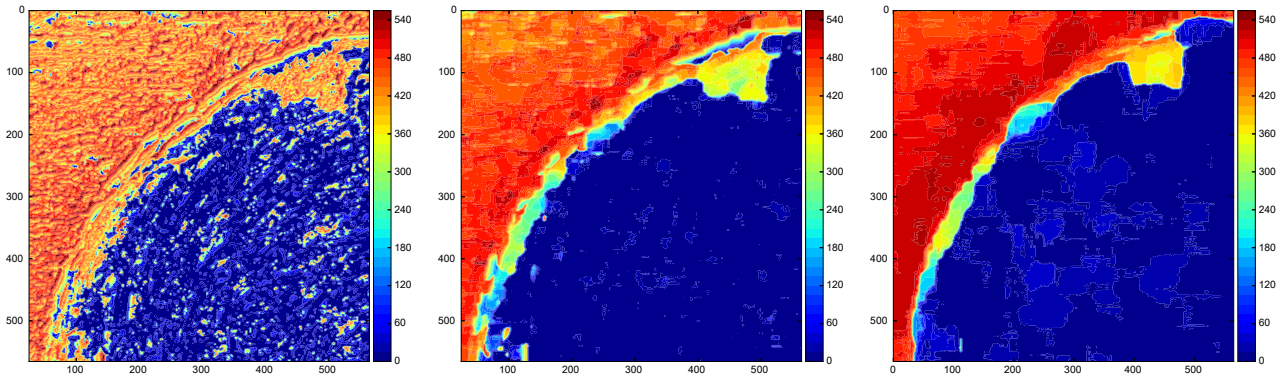

(c) Sum of Squared Difference (SSD), Z resolution = 10µm

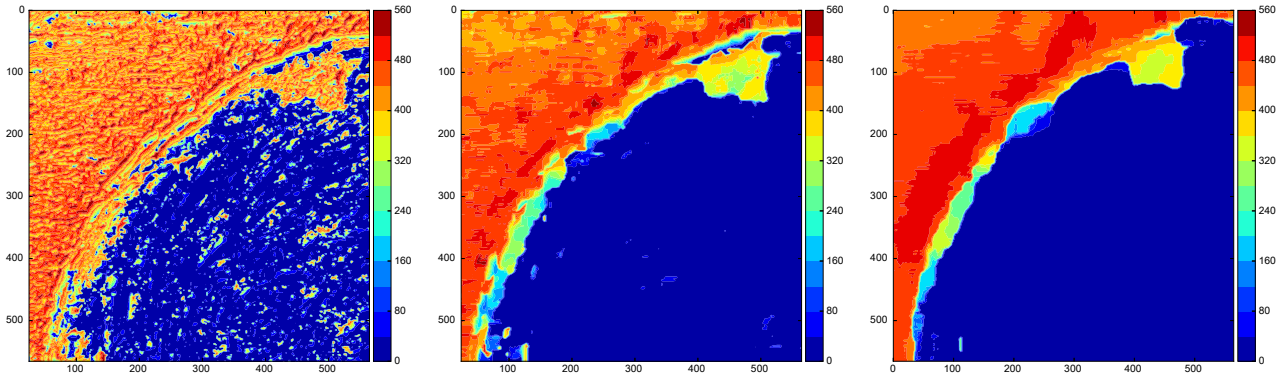

(d) Sum of Squared Difference (SSD), Z resolution = 30µm

Figure 14: Raw dense depth maps for sub-window sizes respectively equal to 5, 15 and 31 pixels, obtained with 3 different focus measures, for either 10µm or 30µm Z resolution. Scales are in µm.

Table 2: Computation time to obtain the depth map of a 500µm high by 640µmx640µm area at 1.6µm resolution in XY and 10µm in z, sub-window size is 31x31 pixels

Focus measure	NGLV	VL	VVL	ML	Ten	VTen	VGL	VSSD	SSD
T(s)	27	133	133	207	208	213	235	260	261

[4] Y. Xiong and S.A Shaffer; Depth from Focusing and defocusing, technical report CMU-RI-TR-93-07 (1993).

[5] P. Favaro and S. Soatto; A Geometric Approach to Shape from Defocus, IEEE Trans. On Pattern Analysis And Machine Intelligence, VOL. 27, NO. 3 (2005).

[6] S. Pertuz, D. Puig, M. A. Garcia, Analysis of focus measure operators for shape-from-focus, Pattern Recognition. 46(5): 1415-1432 (2013).

[7] S. Nayar et al.; Real-time focus range sensor; Proc. of intl. Conf. On Computer Vision; pg 995-1001 (1995).

[8] S. Nayar; Shape from Focus; Carnegie Mellon University Technical report, CMU-RI-TR-89-27 (1989).

[9] S. Nayar and Y. Nakagawa;Shape from focus; IEEE Transactions on Pattern Analysis and Machine Intelligence; 16; pp. 824831 (1994).

[10] C.J.R Sheppard; Depth of Field in Optical Microscopy; Journal of Microscopy, Vol. 149; pp.7375 (1987).

[11] D.B. Murphy, Fundamentals of Light microscopy and Electronic Imaging, Wiley & Sons .

[12] T. Müller, A. Pösch and E. Reithmeier, Ein vereinfachter optischer Aufbau für den Autofokus eines Mikroskops mittels einer verstellbaren Linse, Technisches Messen; 82(3): 145155 (2015).

[13] www.alicona.com.

[14] http://www.keyence.com/ss/products/microscope/vr/spec/.

[15] Optotune, www.optotune.com.

[16] Varioptics, www.varioptics.com.

[17] Diatom autofocusing in brightfield microscopy, J. L. Pech-Pacheco et al, Proc. of 15th International Conf. on Pattern Recognition; pg 314-317. (2000).

[18] Fahrbach et al.; Rapid 3D light-sheet microscopy with a tunable lens; Optics Express Vol. 21; Issue 18; pp. 21010-21026 (2013).

[19] M. Watanabe and S. K. Nayar; Telecentric optics For focus analysis; IEEE Transactions on Pattern Analysis and Machine Intelligence, vol. 19, pg. 1360-1365 (1997).

[20] S. Pertuz, M.A. Garcia and D. Puig, Efficient Focus Sampling Through Depth-of-Field Calibration, Int J Comput Vis 112:342353 (2015).

Author Biography

Ludovic J. Angot-Petit received a technician diploma (BsC) in physics measure from the University Paris XI Orsay, an electrical engineering diploma from the Superior School of Electricity (Supelec), Gif/Yvette France and a PhD from the joint program of University Paris VI Jussieu and Supelec. He has been working at the Industrial Technology Research Institute, Taiwan, since 2007.